DØ Note 6056-CONF

Measurement of the differential cross section $\mathrm{d}\sigma/\mathrm{d}|t|$ in elastic $p\bar{p}$ scattering at $\sqrt{s} = 1.96$ TeV

The DØ Collaboration
URL http://www-d0.fnal.gov
(Dated: April 21, 2010)

A measurement of the $p\bar{p}$ elastic differential cross section, $\mathrm{d}\sigma/\mathrm{d}|t|$, is presented as a function of the four-momentum transfer squared, $|t|$, which is based on $\mathcal{L} \sim 30\ nb^{-1}$ of data collected by the DØ experiment at $\sqrt{s} = 1.96$ TeV, during specialized (low luminosity) Tevatron conditions. In the range $0.25 < |t| < 0.6$ GeV^2 the differential cross section is observed to decay more rapidly than in the range $0.6 < |t| < 1.2$ GeV^2, where a much more gradual decay is observed. A fit of the form $\mathrm{d}\sigma/\mathrm{d}|t| = C\exp(-b|t|)$, performed in the range $0.25 < |t| < 0.6$ GeV^2, yields an exponential slope parameter of $b = 16.54 \pm 0.10(\mathrm{stat}) \pm 0.80(\mathrm{syst})$ GeV^{-2}.

Preliminary Results for Spring 2010 Conferences

I. INTRODUCTION

The elastic differential cross section, $d\sigma(p\overline{p} \to p\overline{p})/d|t|$, contains relevant information about proton structure and non-perturbative aspects of proton (p)-antiproton ($\overline{p}$) interactions. At very low values of $|t|$ ($|t| < 10^{-3}$ GeV^2), where $|t|$ is the $p/\overline{p}$ four-momentum transfer squared ($|t| = (p_f - p_i)^2$, where p_i and p_f are the initial and final four-momentum, respectively), the cross section is dominated by Coulomb scattering, which can be used for obtaining the overall normalization of $d\sigma/d|t|$ [1]. At values of $|t| \approx 10^{-3}$ GeV^2, the interference between Coulomb and nuclear scattering reaches a maximum value. This $|t|$ range can be used to measure ρ, the ratio of the real to the imaginary part of the forward elastic scattering amplitude [2]. At higher $|t|$ values, the nuclear scattering amplitude dominates, and it has been observed that $d\sigma/d|t|$ has a structure with an exponential decay followed by a dip, the first diffraction minimum, after which $d\sigma/d|t|$ continues to decrease [3].

Studies of the center-of-mass energy, $\sqrt{s}$, dependence of $d\sigma/d|t|$ have demonstrated an effect known as shrinkage, namely that the elastic slope becomes larger (steeper) with increasing $\sqrt{s}$, and the $|t|$ value where the dip occurs is reduced [4]. The elastic differential cross section plays an important role in constraining phenomenological models that attempt to explain soft diffractive processes and which cannot be directly calculated by perturbative QCD [5], [6].

Typical elastic scattering angles are very small (less than few milliradians), consequently protons and antiprotons scattered at these angles cannot be detected by the main DØ detector [7]. The scattered protons and antiprotons from elastic collisions are therefore detected with specialized detectors inserted within the beam pipe on either side of the interaction point (IP). For Run IIa, the DØ experiment added a Forward Proton Detector (FPD) to measure scattered protons and antiprotons from elastic and diffractive scattering. In this note we present a preliminary measurement of the p-$\overline{p}$ elastic differential cross section at $\sqrt{s}$=1.96 TeV in the range $0.25 < |t| < 1.2$ GeV^2, measured using the FPD detector of the DØ experiment. Our measurement extends the $|t|$ range previously studied by the Tevatron experiments CDF [8] and E710 [9], and constitutes a first observation of the first diffraction minimum of $d\sigma/d|t|$ at Tevatron energies.

II. FORWARD PROTON DETECTOR OVERVIEW

Figure 1 shows the layout of the FPD [7]. In the center of the diagram is the IP surrounded by the DØ detector. The FPD consists of eight quadrupole spectrometers (plus a dipole spectrometer not shown here). The detectors comprising the quadrupole spectrometers are located at about 23 m and 31 m, adjacent to the electrostatic beam separators, on both the proton side (P) and antiproton side (A) and use the Tevatron quadrupole magnets to obtain the $p/\overline{p}$ scattering angles after reconstructing the $p/\overline{p}$ hits in the scintillating fiber detectors.

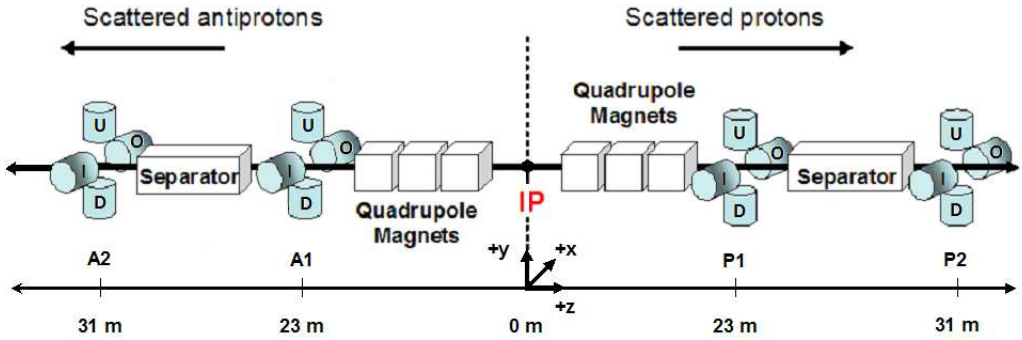

FIG. 1: The layout of the Roman pot stations and Tevatron components comprising the Forward Proton Detector as described in the text (not drawn to scale).

Each spectrometer consists of a pair of detectors, in the same plane: either above (U), below (D), on the inner side (I), or on the outer side (O) of the Tevatron Ring. This combination of spectrometers maximizes the acceptance for protons and antiprotons given the available space for locating the detectors. Particles traverse thin steel windows at the entrance and exit of each Roman pot (the stainless steel vessel that houses each detector)[10]. The pots were remotely controlled and moved close to the beam (within a few mm) during stable beam conditions.

Each position detector consists of three planes of scintillating fibers, each with two layers (U, U', V, V', X, X'), where the U,U' and V,V' planes are rotated by plus or minus 45 degrees from the vertical X,X' fibers, and the "primed"

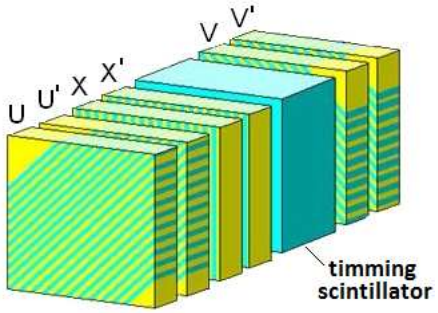

FIG. 2: Schematic of one FPD scintillating fiber detector.

planes were offset by two-thirds of a fiber (0.53 mm) from the "unprimed" planes (see figure 2). The detector uses 0.8 mm × 0.8 mm square double-clad plastic scintillating fibers to detect the passage of charged particles. Outside of the detector active area, matching square clear fibers transport the scintillator signals to 16 channel multi-anode photomultiplier tubes. The electronic signals are subsequently amplified, shaped, and sent to the DØ triggering and data acquisition system. FPD triggers were based on fiber information that passed a signal threshold of the FPD Analog Front-End boards. The FPD trigger equations were all based on "wide" fiber segments (width of about 1.1 mm) which combined the primed and unprimed planes.

Each detector also contained a scintillator which was read out by a Time-to-Digital Converter (TDC) system based on the DØ Luminosity Monitor (LM) electronics [7]. In addition to providing a time measurement for particles that passed through the detector in a time-window consistent with the scattered proton/antiproton outgoing time-of-flight from the collision point, the TDC system also set a halo flag for particles in an earlier incoming time-window. Halo particles are particles traveling far enough outside of the main beam core that they can pass through the detectors and be mistaken for elastic or diffractive protons and antiprotons. If these halo particles arrive at the proton detectors at the time expected for an in-time proton, frequently they have passed through the diagonally opposite antiproton detectors at an earlier time (and vice versa).

III. ELASTIC ANALYSIS

The analysis consists of the following steps which are discussed in detail below. First, the elastic data sample is obtained using the elastic triggers. Hits are reconstructed from the fibers that are ON, and the hits are then used to select elastic candidate events. In order to reconstruct the path of the protons and antiprotons through this region of the Tevatron, we align the detectors with respect to the beam and then use the beam transport matrices for the track reconstruction. At this point, we introduce a Monte Carlo (MC) simulation to perform corrections for acceptance, detector resolution and beam divergence effects. Finally we do background subtraction and efficiency corrections.

A. Data Sample

The data for this analysis were taken in February 2006 in a dedicated store with special conditions designed to facilitate the positioning of the FPD Roman Pots as close to the beam axis as possible. The Tevatron injection tune with the lattice parameter β^*=1.6 m at the DØ IP was used instead of the standard β^*=0.35 m lattice [11]. There was only one proton bunch colliding with one antiproton bunch. Scraping in the vertical and horizontal planes was performed to remove the halo tails of the beams and the electrostatic separators were turned off for this store . The initial instantaneous luminosity was about 0.5×10^{30} cm^{-2}s^{-1} and the initial beam emittances were 17 and 20 π mm-mrad for the $\overline{p}$ and p beams, respectively. The recorded luminosity of this store was about 30 nb^{-1}, which is divided in two data sets corresponding to two different detector positions. Approximately 20 million events were recorded using a special trigger list optimized for diffractive physics, including triggers for elastic, single diffractive, and double pomeron configurations. This analysis is based primarily on the elastic triggers, which comprised about 25% of the total data sample.

Elastic triggers are defined by the logical OR ($\oplus$) of the four possible elastic combinations of diagonally opposite spectrometers: $A_U P_D \oplus A_D P_U \oplus A_I P_O \oplus A_O P_I$, where A_U stands for the coincidence of the detectors A_{1U} and A_{2U} (similar definition is used for the other spectrometers). During the course of the store, several different conditions on the detector hits were employed in the trigger: a Tight (T) trigger that demanded a single three-plane hit in

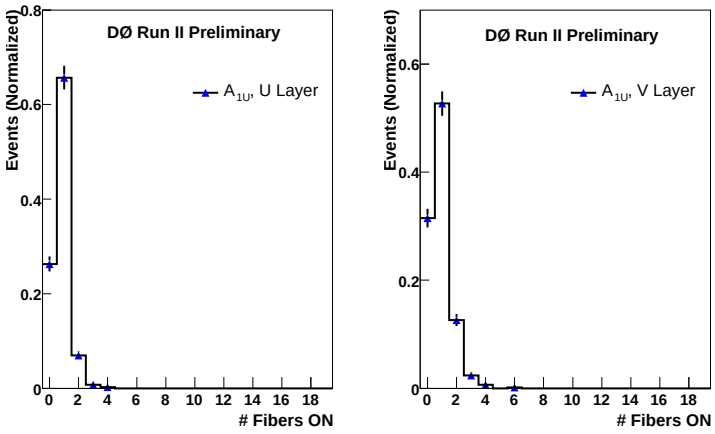

FIG. 3: Fiber multiplicity distributions for single particles in the U and V fiber layers of A_{1U} detector. Similar distributions are observed for all detectors.

the detector, a Medium (M) trigger that allowed up to three hits, and a Loose (L) trigger that allowed hits to be comprised of two out of the three planes.

B. Hit Reconstruction

A fiber is considered to be ON if its associated signal is above the input signal threshold to the FPD trigger system. To reconstruct a hit offline, for each fiber ON we check if there is an adjacent fiber ON in the primed layer in order to define a "fine" fiber segment where the particle traversed the plane. Figure 3 shows typical fiber multiplicity distributions for single particles going through a fiber layer of a detector. Events with more than four fibers ON in a plane are typically not due to single particles and are rejected. We require at least two fiber segments, from different fiber planes, to be reconstructed in each detector, with their intersection yielding the (x, y) coordinates of the hit. We then make a list of all possible hits in a detector. In the case of more than one hit in a detector, we weight the hits by the sum of the Analog-to-Digital Converter (ADC) counts of all the fibers that contributed in the reconstruction of the hit, and use the hit with the highest ADC weight. We have varied the hit definition, and have chosen this one as it maximizes the number of reconstructed elastic events. The selection efficiency correction accounts for elastic events that are discarded by this definition.

Utilizing events with hits in all three fiber planes, we are able to estimate the position resolution of the detector by taking the difference between x coordinate obtained from UV fiber intersection and a similar measurement using the X fiber plane. A typical detector used in this analysis has a coordinate resolution of about $\sigma = 185\mu$m (see figure 4).

C. Selection of Candidate Elastic Events

Elastic candidate events are required to have hits in all four of the detectors comprising an "elastic" configuration, $A_U P_D$ or $A_D P_U$. The elastic configurations $A_I P_O$ and $A_O P_I$ have very poor acceptance for elastic events and are only used for alignment purposes. We observe a definite correlation band from particles going through a spectrometer, but also observe some uncorrelated background events. We require a 3σ band cut to select only the events inside the diagonal correlation band in each spectrometer. Then we look at the correlation between the coordinates of the protons and antiprotons in diagonally opposite spectrometers corresponding to the possible elastic configurations. In addition to the expected correlation due to the co-linearity of elastic events, some background contamination due to halo particles is observed. This halo contamination is reduced through the use of the FPD timing system described above, but there is still some residual background, partially due to inefficiency of the trigger scintillator and different acceptance of the spectrometers. The former is further reduced by band cuts, and the latter by fiducial cuts (discussed below) that equalize the detector acceptance. The remaining halo contribution within the correlation band is subtracted using the FPD timing system (see section III E).

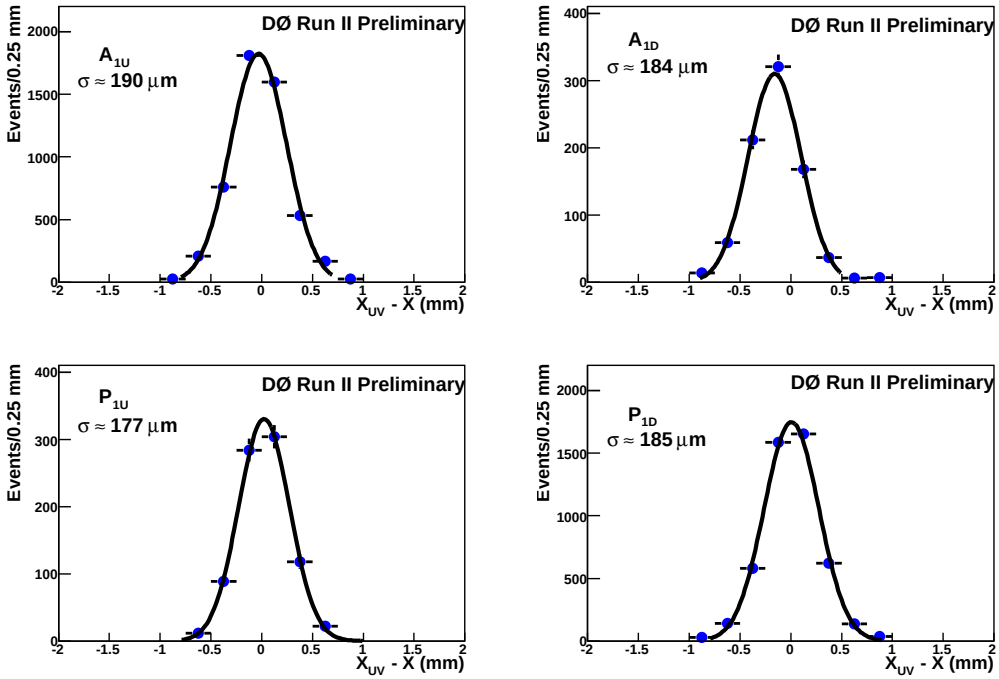

FIG. 4: Distributions of $\Delta X = X_{UV} - X$ for detectors A_{1U}, A_{1D}, P_{1U}, P_{1D}. The resolution, σ, of a detector is found as $\sigma = \Delta X/\sqrt{2}$.

For a specific set of p and $\overline{p}$ spectrometers that comprise an elastic combination we observe that elastic events with a proton passing through a small region of the detectors in one spectrometer will have $\overline{p}$ positions distributed over a similar but somewhat larger region of the diagonally opposite spectrometer. Depending on the location of the proton, this Gaussian distribution of the $\overline{p}$ position may be truncated due to the finite detector size. After calculating this acceptance correction, as a function of the coordinates of the proton spectrometer, a fiducial cut is applied to only use regions which require a correction of 2% or less. We only apply those fiducial cuts in the P_1 detectors, since they have the best resolution. The region we choose in the P_1 detectors is thus guaranteed to have an acceptance greater than 98% for the other three detectors. Figure 5 shows the y_p vs $y_{\overline{p}}$ correlation plots (y measured with respect to the bottom of the detectors), the effect of the tagging of the hits according to time of flight information and the fiducial cuts applied. We also check that there is no activity in the calorimeter for the elastic sample selected. The contribution to the elastic sample from events that have a non-zero energy in the calorimeter is found to be less than 1%. The fraction of events with multiple interactions is negligible given the low luminosity for our data taking.

D. Track Reconstruction

In order to reconstruct tracks, we first align the detectors with respect to the beam, and then determine the position and angle of a particle at the IP from the measured position in the FPD detectors through the application of Tevatron transport matrices, obtained from the Fermilab Accelerator Division [11].

1. Alignment

To obtain the scattering angle and its corresponding $|t|$ value, we need to determine the location of the detectors with respect to the beam. Since the detectors were very close to the beamline, there is a sample of tracks that pass through both the vertical and horizontal detectors, which allow the determination of the relative alignment of the detectors. We define the center of a vertical and a horizontal pot at each Roman pot station and then measure the positions of all four pots with respect to this reference system. Then we determine the beam offset in x for the vertical proton detectors and the beam offset in y for the horizontal antiproton detectors, by finding the center of the x and

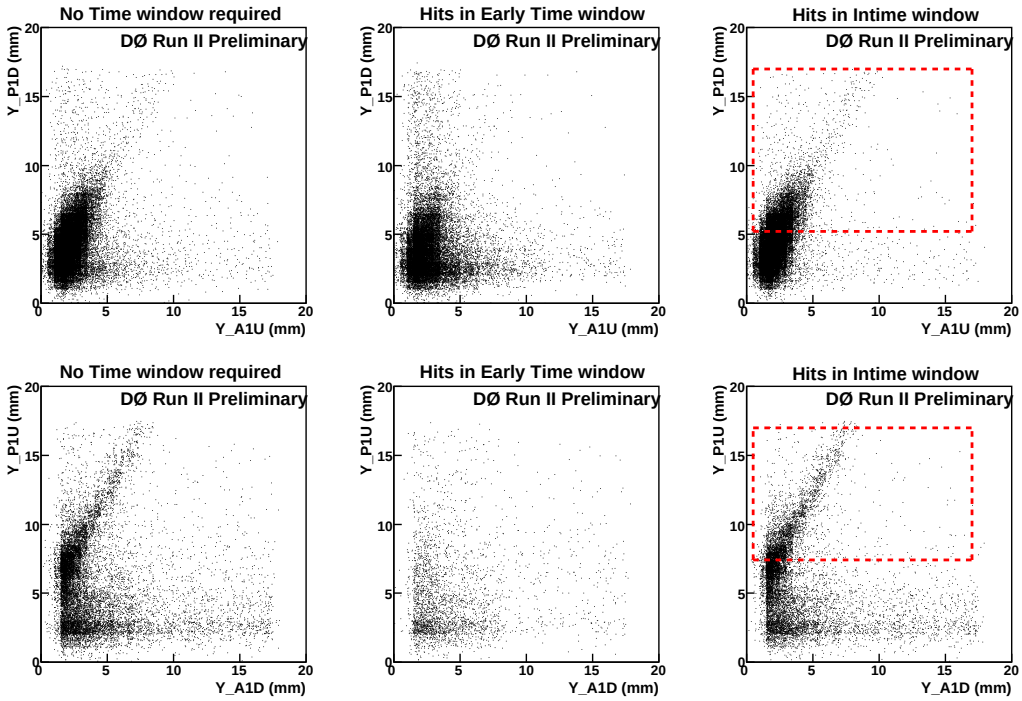

FIG. 5: y_p vs $y_{\overline{p}}$ correlation plots (y coordinates measured from the bottom of the detectors). The upper row corresponds to elastic combination AUPD and the lower row to ADPU. The first column shows the correlations without any timing requirement. The second column corresponds to hits within the early time window and the third column shows the hits within the in time window. The dashed lines shown in the third column correspond to the fiducial cuts applied.

y distributions in these detectors. All other beam offsets can be obtained if we use an elastic sample, given the fact that the reconstructed IP offset and scattering angle should be the same for both the proton and antiproton that comprise the elastic event. We take the average over all four elastic combinations as the offset of the beam at each Roman pot station. The uncertainty in the alignment obtained with this procedure is about 100 μm for both x and y coordinates. In Fig. 6, we show the locations of the pots with their positions obtained with the alignment procedure described above for the data set corresponding to the detector configuration with Roman pots located closest to the beam (data set 2). The coordinates are plotted with respect to the beam coordinate system (dashed lines shown in the plot). To align the data set where most of the detectors were farther from the beam (data set 1), we use the position difference information from the pot motion system added to the previously determined aligned positions. The pot motion system has been independently determined to be linear, reproducible, and accurate to the 10 μm level.

2. *Tracking Using Transport Matrices*

The Tevatron transport matrices, which are a function of the currents of the magnets located between the IP and our detectors, are unique for this special store, due to the use of the injection tune without the low beta squeeze. The beam width ranges from 0.4 mm to 0.8 mm at the different FPD detector locations while the beam divergence is about 44 μrad.

The beam spot size in x and y is typically determined by measuring the primary vertex using the silicon microstrip tracker [7]. For elastic events, there is no reconstructed vertex, so other triggers are used to determine the spot size.

To tag an elastic event, we reconstruct coordinates in two antiproton and two proton detectors. The difference of coordinates between two detectors yields a Gaussian distribution with a width related to the resolution of the two detectors, the beam spot size, and the beam divergence. Since we have already measured our detector resolutions and the beam spot size, we use the distributions of the difference in coordinates of two detectors to estimate the beam divergence, and obtain a value similar (40 ± 5 μrad) to that calculated above.

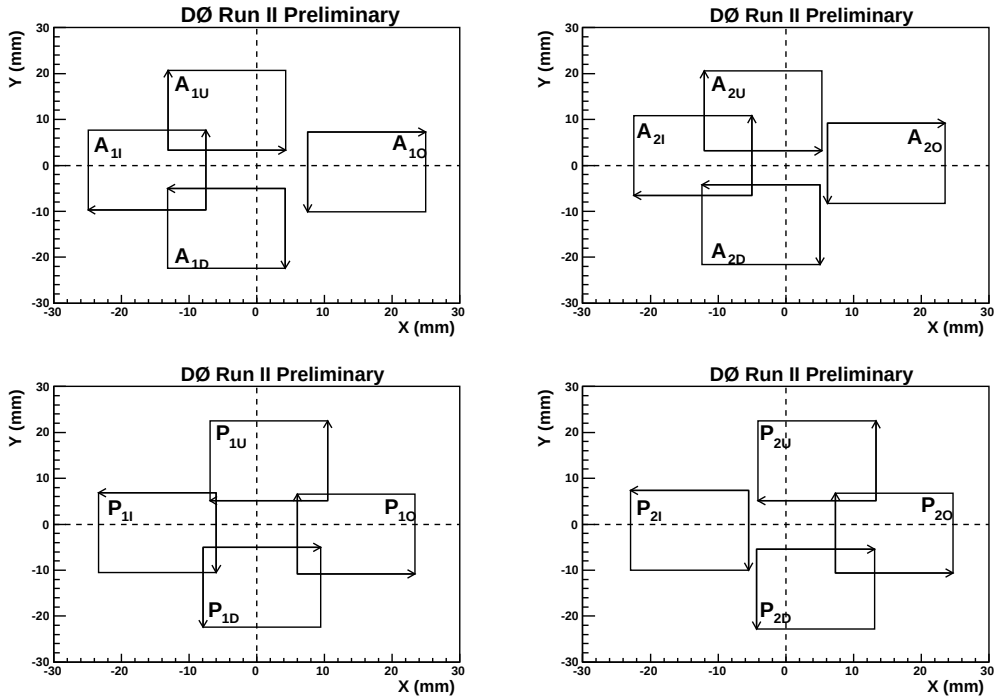

FIG. 6: Pot positions, with respect to beam center (dashed lines), for the data set corresponding to the closest pot insertion to the beam. The arrows indicate the local coordinate system in each pot.

3. $|t|$ Measurement

Using the transport matrices, for the Tevatron optics used for our data taking, one can find the IP offset and the scattering angle at the IP. With the scattering angle, we can determine the four-momentum transfer squared, $|t|$. Because we have selected a clean sample of elastic events, we take the momentum of the elastically scattered proton and antiproton to be 980 GeV, so the uncertainty in $|t|$ only comes from the uncertainty in the scattering angle. Figure 7 shows the difference in the reconstructed $|t|$ from the p and $\overline{p}$ vertical spectrometers, $\Delta|t| = |t|_{\overline{p}} - |t|_p$. The standard deviation of $\Delta|t|$ is due to the resolution of $|t|_p$ and $|t|_{\overline{p}}$. The average of $|t|_p$ and $|t|_{\overline{p}}$ ($|t|_{ave} = (|t|_p + |t|_{\overline{p}})/2$) will have a resolution of approximately $\sigma_{\Delta|t|}/2$ which defines the minimum bin size we use for our result. We have also studied the dependence of the $|t|$ resolution as a function of $|t|$, and observe a gradual increase with $|t|$, from 0.02 GeV^2 to 0.04 GeV^2, that is reflected in our final bin size for the dσ/d$|t|$ distribution.

E. Background Subtraction

The primary source of background to elastic events is due to halo contamination, consisting for example of two simultaneously reconstructed halo proton and halo antiproton events, or a halo event combined with a single diffractive event. As described earlier, timing information is very useful to veto events with early time hits, consistent with contamination from halo protons and antiprotons in the elastic sample. The veto is not 100% efficient due to a combination of scintillator inefficiency and different positioning of the detectors with respect to the beam (a closer detector position both increases a detector's acceptance and changes its ability to reject halo in the diagonally opposite spectrometer), consequently it is necessary to subtract the residual background. We consider that there is $\overline{p}$ halo if one or both of the two $\overline{p}$ detectors (in the elastic combination) have hits in the halo timing window; a similar condition is applied for the proton spectrometer. We only accept a signal event to be a good elastic candidate if neither the p_{halo} nor the $\overline{p}_{halo}$ timing windows have activity. We also build a background sample requiring that both the p_{halo} and $\overline{p}_{halo}$ timing windows are ON. To subtract the background, we first establish that the signal events outside the elastic correlation band have $|t|$ distributions consistent in shape with the background events out of the diagonal band. We take the ratio of those two numbers and use it to normalize background events inside the elastic band, and then subtract the normalized background events from signal events inside the elastic band to obtain the dN/d$|t|$ used in our measurement. The amount of background subtracted inside the elastic correlation band is less than 5% of the

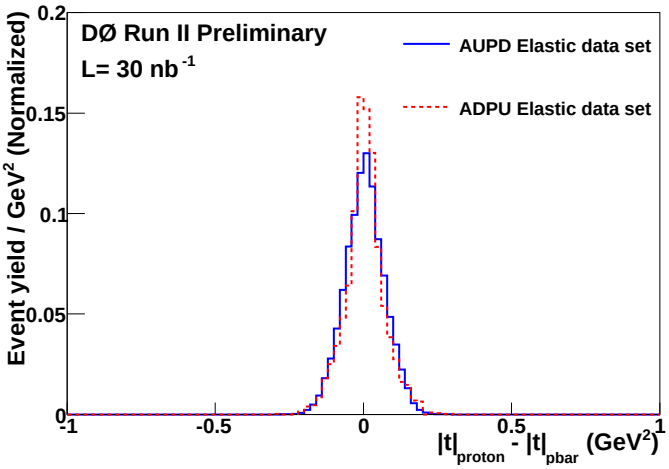

FIG. 7: Difference in the reconstructed $|t|$ between p and $\overline{p}$ vertical spectrometers. The solid line corresponds to elastic events reconstructed with the $A_U P_D$ combination and the dashed line for the $A_D P_U$ combination. The distributions are normalized to unity.

signal.

F. Monte Carlo Simulation of Elastic Events

We use a standalone MC program based on the Tevatron transport matrices to simulate elastic events in the FPD. The MC includes the 16 quadrupole detector positions and allows us to study the geometrical acceptance of the detectors, resolution smearing, alignment, and effects from beam spot and beam divergence at the IP. The generation of events is based on an ansatz function that we obtain by fitting the $\mathrm{d}\sigma/\mathrm{d}|t|$ distribution of our data. We studied the various corrections using signal generated with a wide range of different $\mathrm{d}\sigma/\mathrm{d}|t|$ distributions. The variations in the corrections are quoted as systematic uncertainties.

The particles produced at the IP are propagated through the beam lattice to the detector locations using the beam transport matrix elements. The position of the hit in the detector is transformed to fibers, and the reconstruction proceeds using the hit fibers, following the same procedure as with the real data. The simulated correlation patterns are in good agreement with those observed in data. In addition, the simulation also predicts the width of the different correlations reasonably well as it is shown in figure 8.

G. Acceptance and Bin Smearing Correction

Each detector has a different coverage in azimuthal angle ϕ (and therefore a different coverage of azimuthal ellipses of constant $|t|$, which the scattered particles occupy on their way out from the IP). The ϕ acceptance correction corresponds to the fraction of the $|t|$ ellipse for each $|t|$ bin that is covered by the fiducial area used in the detector. This correction depends only on the detector location with respect to the particle beam and the geometry of fiducial area used in the detector for selecting events. Figure 9 shows the calculated ϕ acceptance correction as a function of $|t|$, for data taken at the closest detector position with respect to the beam, after fiducial cuts (explained in section III C). Because the fiducial cuts guarantee that the other three detectors have full acceptance, we only need to find the ϕ acceptance of the P1 detectors, which are the ones where we define the fiducial cuts. We obtain similar results for the ϕ acceptance correction using the MC described in the previous section. To obtain the $|t|$ bin smearing (mainly caused by beam divergence and detector resolution) correction factor we add the measured value of beam divergence and detector resolution to the MC and take the ratio of the reconstructed $\mathrm{d}N/\mathrm{d}|t|$ to the $\mathrm{d}N/\mathrm{d}|t|$ obtained from a MC with no smearing. This factor is used to correct the $\mathrm{d}N/\mathrm{d}|t|$ distribution obtained from data. In the systematic uncertainties, we quote the error from the uncertainty in the choice of ansatz function as well as the uncertainty in beam divergence.

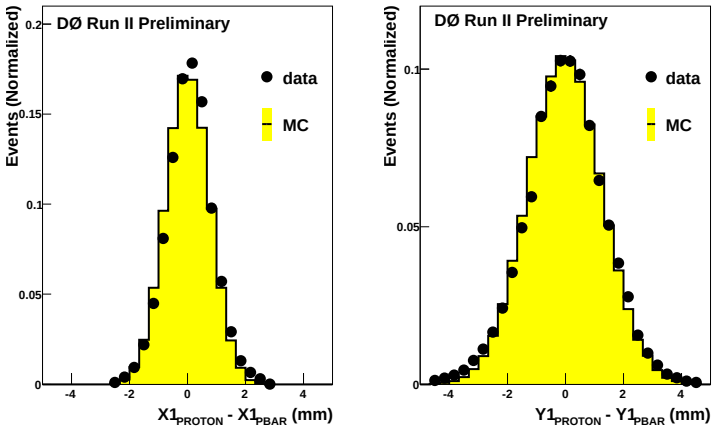

FIG. 8: Comparison of MC (solid line) and data (black points) for distributions of X_p - $X_{\overline{p}}$ and Y_p - $Y_{\overline{p}}$ for first detectors of the elastic configuration AUPD.

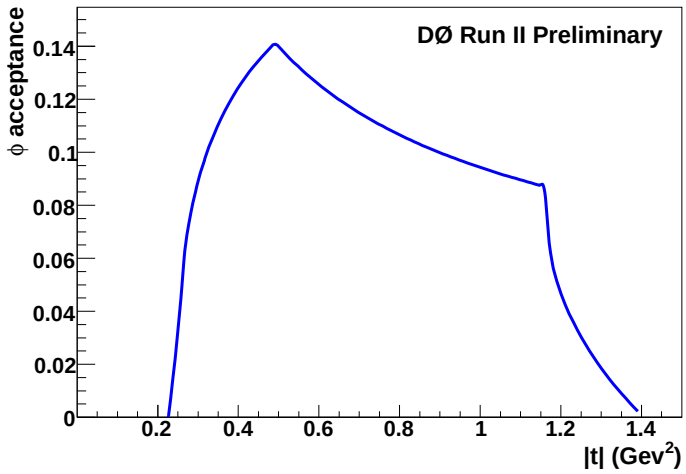

FIG. 9: DØ FPD ϕ acceptance, after fiducial cuts, for the closest detector position.

H. Selection and Trigger Efficiencies

We determine simultaneously the effect of both the selection and trigger efficiencies in a single efficiency number for each of the four detectors comprising an elastic combination. To determine the efficiency of a particular detector, we use an independent trigger that does not include that specific detector. Then we reconstruct the hits in the other three detectors, applying the different filters to select elastic events. We then plot the $\mathrm{d}N/\mathrm{d}|t|$ distribution in the case of the three detectors with an elastic track reconstructed and in the case of all four detectors with an elastic track and with the trigger condition satisfied. The ratio of the two distributions give us the efficiency of the detector of interest as a function of $|t|$, where $|t|$ is reconstructed from the coordinates of the opposite side spectrometer. To avoid any acceptance issue, we only accept hits in the other three detectors in a region we know has full acceptance in the detector of interest. We repeat a similar procedure for each of the four detectors in every elastic combination and multiply the efficiencies of the four detectors to determine the final efficiency correction to $\mathrm{d}\sigma/\mathrm{d}|t|$. Typical detector efficiencies are in the range of 50% to 70% depending on the detector and trigger condition.

IV. MEASUREMENT OF $\mathrm{d}\sigma/\mathrm{d}|t|$

To obtain $\mathrm{d}\sigma/\mathrm{d}|t|$ we apply the acceptance (A) and efficiency (ϵ) corrections to each bin of the raw $\mathrm{d}N/\mathrm{d}|t|$ and scale by the integrated luminosity (L):

$$\frac{d\sigma}{d|t|} = \frac{1}{L \times A \times \epsilon} \frac{dN}{d|t|} \tag{1}$$

The acceptance correction (A) includes the ϕ acceptance plus the $|t|$ bin smearing correction. Since the elastic data was taken with different Tevatron conditions as compared to standard DØ experiment operations, the usual algorithms that are ordinarily used to determine luminosity are not appropriate for our data. To determine the integrated luminosity for our data taking period, we developed a method that compares the number of inclusive jets obtained from our data to the number from Run IIa [12], and note that this ratio should be equal to the ratio of the luminosities, given that various factors such as the energy scale are common to the two running periods, accounting for the different vertex factors. The corresponding integrated luminosities for the two data samples used in this analysis are 18.3 nb^{-1} and 12.6 nb^{-1}, respectively. The uncertainty in the measurement of these luminosities is 13 % and we have to add in quadrature the 6.1 % uncertainty in the luminosity determination of Run IIa, giving an overall normalization error of 14.3 %.

V. RESULTS

The major contributors to the systematic uncertainty of $\mathrm{d}\sigma/\mathrm{d}|t|$ are uncertainties from detector positions, detector efficiencies, beam divergence, ansatz function, and the luminosity measurement. Tevatron beam lattice parameters are known with high precision and therefore produce a much lower uncertainty in our results compared to the other sources. The uncertainty in pot positions from the alignment procedure is estimated to be about 100 μm. We take in the MC the pot position uncertainty as an extra smearing factor of the hit coordinate from the beam center. Since the efficiencies vary with $|t|$, we fit either a polynomial or an exponential function to each trigger efficiency, and propagate the uncertainties in the fit parameters to $\mathrm{d}\sigma/\mathrm{d}|t|$, using the covariance matrix from the fit. For the beam divergences term, we run the MC varying the beam divergence by $\pm$ 5 μrad and we then determine the change in acceptance correction bin-by-bin, and propagate this change to $\mathrm{d}\sigma/\mathrm{d}|t|$. We also consider 26 possible variations of the ansatz function used in the MC to account for the uncertainties in the slopes before and after the dip and also for the $|t|$ value where the change in slope is produced. The 14.3 % error in the luminosity is not included in the plots. We are also including as a systematic uncertainty the difference we observe on $\mathrm{d}\sigma/\mathrm{d}|t|$ obtained from different trigger and detector configurations (added in quadrature to the other sources of systematic uncertainties). In total, we have four measurements of $\mathrm{d}\sigma/\mathrm{d}|t|$ that come from the two elastic combinations ($\mathrm{A_U P_D}$ and $\mathrm{A_D P_U}$) and the two data sets. We combine the four measurements by doing a bin-by-bin weighted average. The $|t|$ range covered by our measurement is $0.25 < |t| < 1.2$ GeV^2. Table I shows the values of $\mathrm{d}\sigma/\mathrm{d}|t|$ with their respective uncertainties we are obtaining. We observe within this $|t|$ range a drastic change in slope in $\mathrm{d}\sigma/\mathrm{d}|t|$ distribution at $|t| \approx 0.6$ GeV^2. The slope of the $\mathrm{d}\sigma/\mathrm{d}|t|$ distribution in the range $0.25 < |t| < 0.6$ is fitted, with an exponential function of the form $C\exp(-b|t|)$, and the extracted value of the slope parameter is $b = 16.54 \pm 0.10$ (stat) ± 0.80 (syst) GeV^{-2}. The major source for the systematic uncertainty in b is found by a comparison of different detectors and trigger conditions. Figure 10 shows our $\mathrm{d}\sigma/\mathrm{d}|t|$ measurement including the best exponential fit. Figure 11 shows a comparison of our measured $\mathrm{d}\sigma/\mathrm{d}|t|$ at $\sqrt{s} = 1.96$ TeV to the values measured at 1.8 TeV by the Tevatron CDF [8] and E710 [9] experiments. The slope parameter measured by these two experiments is in agreement with our measurement.

Our measurement extends the $|t|$ range previously studied by CDF and E710 experiments and provides a first measurement of the first diffraction minimum of the elastic differential cross section, $\mathrm{d}\sigma/\mathrm{d}|t|$, at Tevatron energies. When comparing our result to similar measurements at lower energies, [13], [14], we conclude that the position of the first diffraction minimum keeps moving towards lower values of $|t|$ as the energy increases (see figure 12).

VI. ACKNOWLEDGEMENTS

We thank the staffs at Fermilab and collaborating institutions, and acknowledge support from the DOE and NSF (USA); CEA and CNRS/IN2P3 (France); FASI, Rosatom and RFBR (Russia); CNPq, FAPERJ, FAPESP and FUNDUNESP (Brazil); DAE and DST (India); Colciencias (Colombia); CONACyT (Mexico); KRF and KOSEF (Korea); CONICET and UBACyT (Argentina); FOM (The Netherlands); STFC and the Royal Society (United

TABLE I: Preliminary values of $d\sigma/d|t|$ measured by DØ experiment. The statistical and systematic uncertainties are added in quadrature. A normalization uncertainty of 14.3% is not included.

$\|t\|$ (GeV^2)	$d\sigma/d\|t\|$ (mb/GeV^2)	Total Uncertainty (mb/GeV^2)
0.26	39.7×10^{-1}	7.15×10^{-1}
0.30	18.8×10^{-1}	2.23×10^{-1}
0.34	9.32×10^{-1}	1.23×10^{-1}
0.38	5.03×10^{-1}	8.06×10^{-2}
0.42	2.76×10^{-1}	5.13×10^{-2}
0.46	1.31×10^{-1}	3.16×10^{-2}
0.50	6.85×10^{-2}	1.90×10^{-2}
0.54	3.51×10^{-2}	1.28×10^{-2}
0.58	2.15×10^{-2}	1.04×10^{-2}
0.64	9.91×10^{-3}	4.28×10^{-3}
0.72	9.62×10^{-3}	4.68×10^{-3}
0.80	6.91×10^{-3}	3.99×10^{-3}
0.88	1.07×10^{-2}	5.42×10^{-3}
0.96	7.67×10^{-3}	4.52×10^{-3}
1.04	7.43×10^{-3}	4.82×10^{-3}
1.12	6.23×10^{-3}	4.30×10^{-3}
1.20	3.38×10^{-3}	5.22×10^{-3}

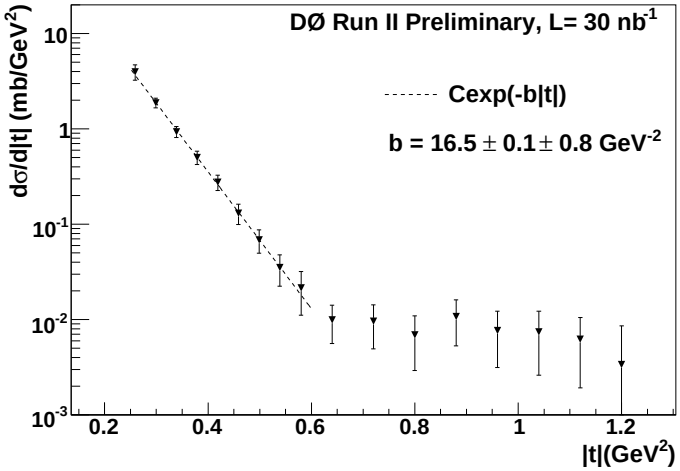

FIG. 10: $d\sigma/d|t|$ with its corresponding exponential fit. A normalization uncertainty of 14.3% is not shown. The uncertainties on the points are obtained by adding in quadrature statistical and systematic uncertainties.

Kingdom); MSMT and GACR (Czech Republic); CRC Program and NSERC (Canada); BMBF and DFG (Germany); SFI (Ireland); The Swedish Research Council (Sweden); and CAS and CNSF (China).

[1] N. Amos *et al.* Nucl. Phys. B **262** 689 (1985).
[2] M. Block and R. Cahn., Rev. Mod. Phys. **57** 563 (1985).
[3] G. Giacomelli, Phys. Rep. **23**, 123 (1976).
[4] G. Alberi, G. Goggi, Phys. Rep. **74** 1 (1981).
[5] *High Energy Particle Diffraction*, V. Barone, E. Predazzi, Springer,2002.
[6] *Quantum Chromodynamics and the Pomeron*, J. Forshaw and D.A. Ross, Cambridge Lectures notes in Physics, 1997.
[7] M. Abazov *et al.* (D0 Collaboration), Nucl. Instr. and Methods Phys. Res. A **565** 463 (2006).
[8] F. Abe *et al.* (CDF Collaboration), Phys. Rev. D **50** 5518 (1994).
[9] N. Amos *et al.* (E710 Collaboration), Phys. Lett. B **247** 127 (1990).
[10] U. Amaldi *et al.* Phys. Lett. B **44** 112 (1973).

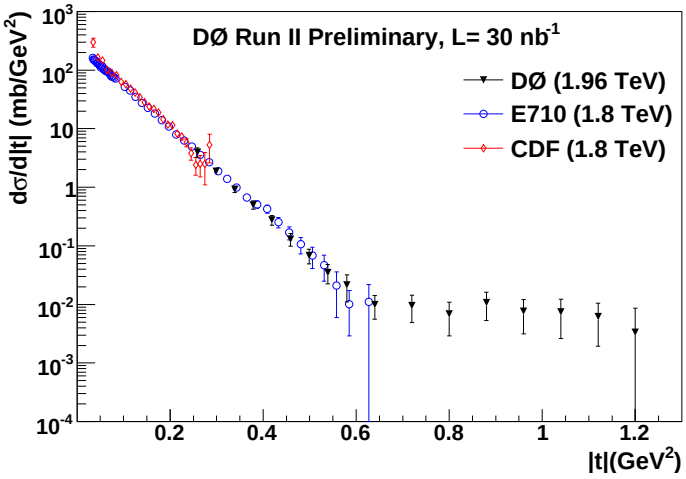

FIG. 11: $d\sigma/d|t|$ measured by DØ experiment and compared to CDF and E710 measurements at 1.8 TeV. A normalization uncertainty of 14.3% is not shown. The uncertainties on the points are obtained by adding in quadrature statistical and systematic uncertainties.

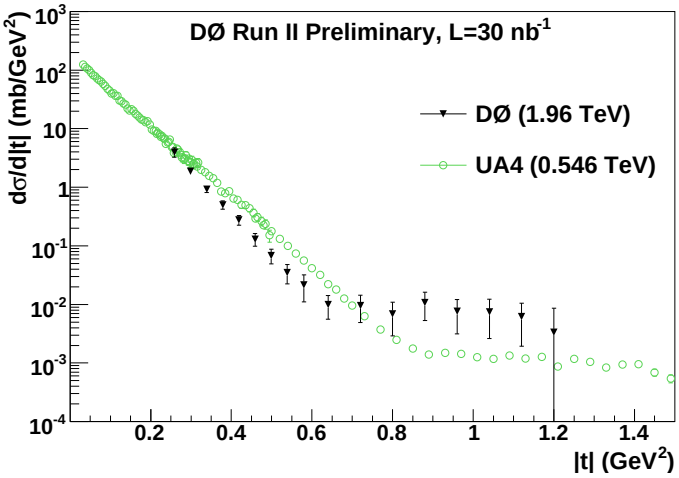

FIG. 12: $\frac{d\sigma}{dt}$ measured by DØ experiment and compared to UA4 measurement.

[11] http://www-bdnew.fnal.gov/tevatron/data.html.
[12] M. Abazov *et al.* (D0 Collaboration), Phys. Rev. Lett. **101** 062001 (2008).
[13] M. Bozzo *et al.* (UA4 Collaboration), Phys. Lett. B **147** 385 (1984).
[14] M. Bozzo *et al.* (UA4 Collaboration), Phys. Lett. B **155** 197 (1985).